



1 **Assessments of land subsidence along Rizhao-Lankao High-speed Railway at Heze,**  
2 **China between 2015 and 2019 with Sentinel-1 data**

3

4 Chuanguang Zhu<sup>1</sup>, Wenhao Wu<sup>1</sup>, Mahdi Motagh<sup>2,3</sup>, Liya Zhang<sup>1</sup>, Zongli Jiang<sup>1</sup>, and Sichun Long<sup>1</sup>

5 <sup>1</sup>Key Laboratory of Coal Resources Clean-utilization & Mine Environment Protection of Hunan Province, Hunan university  
6 of Science & Technology, Xiangtan 411201, China

7 <sup>2</sup>Section of Remote Sensing and Geoinformatics at GFZ German Research Centre for Geosciences in Potsdam, Germany

8 <sup>3</sup>Institute of Photogrammetry and Geoinformation at Leibniz University Hannover (LUH) in Hannover, Germany

9

10 *Correspondence to:* Chuanguang Zhu ([zhucg@hnust.edu.cn](mailto:zhucg@hnust.edu.cn))

11

12 **Abstract.** The Heze section of Rizhao-Lankao High-speed Railway (RLHR-HZ) has been under  
13 construction since 2018 and will be operative by the end of 2021. However, there is a concern that land  
14 subsidence in Heze region may affect the normal operation of RLHR-HZ. In this study, we investigate the  
15 contemporary ground deformation in the region between 2015 and 2019 by using more than 350 C-band  
16 interferograms constructed from two tracks of Sentinel-1 data over the region. The Small Baselines Subset  
17 (SBAS) technique is adopted to compile the time series displacement. We find that the RLHR-HZ runs  
18 through two main subsidence areas: One is located east of Heze region with rates ranging from -4 cm/yr to  
19 -1 cm/yr, and another one is located in the coal field with rates ranging from -8 cm/yr to -2 cm/yr. A total  
20 length of 35 km of RLHR-HZ are affected by the two subsidence basins. Considering the previous  
21 investigation and the monthly precipitation, we infer that the subsidence bowl east of Heze region is due to  
22 massive extraction of deep groundwater. Close inspections of the relative locations between the second  
23 subsidence area and the underground mining reveals that the subsidence there is probably caused by the  
24 groundwater outflow and fault instability due to mining, rather than being directly caused by mining. The  
25 InSAR-derived ground subsidence implies that it's necessary to continue monitoring the ground  
26 deformation along RLHR-HZ.

27

28 **1 Introduction**

29 The Heze region, lying in the North China Plain, has been adversely affected for decades by ground  
30 subsidence, mainly caused by the soil compaction and consolidation due to the excessive exploitation of  
31 aquifer (Cui 2018; Hu et al., 2004; Guo et al., 2019; Xue et al., 2005). To slow down the subsidence, the  
32 local governments have proposed new regulations on exploitation of groundwater. However, the extraction  
33 of groundwater is still greater than recharge due to the urban sprawl and industrial development, which  
34 results in continuous ground subsidence. In addition, underground mining activities have also exacerbated  
35 the problems of subsidence in recent years (Wang 2014; Yang et al., 2010). The resulting subsidence has



1 already caused some environment hazards, e.g., collapse of roads, buildings and other infrastructures (Yue  
2 2020).

3 The RLSR-HZ, with a length of 150 km and a speed of 300 kph, has been under construction since  
4 December 2018 and will be operative by the end of 2021. The ground subsidence may menace the  
5 RLSR-HZ and therefore currently is a matter of major safety concern. It is crucial to monitor ground  
6 deformation along the RLSR-HZ to avoid potential hazards in future.

7 Field-survey based on a few sparse points, such as spirit leveling and global position system (GPS) are  
8 the main methods for measuring ground deformation in Heze region. However, it is difficult to obtain  
9 detailed and comprehensive deformation based on these sparse points. Moreover, these geodetic  
10 measurements are very timing consuming and highly labor intensive, especial for the RLSR-HZ extending  
11 over a large region. More advance methods are required to retrieve the latest temporal and spatial evolution  
12 of ground deformation along the RLSR-HZ.

13 The multi-temporal Interferometric Synthetic Aperture Radar (MT-InSAR), such as Persistent Scatter  
14 Interferometry (PSI) (Ferretti et al., 2000, 2001; Hooper et al., 2007; Kampes, 2006) and Small Baseline  
15 Subset (SBAS) algorithm (Berardino et al., 2002; Hooper 2008; Mora et al., 2003), is a powerful tool for  
16 producing measurements of deformation with high precision and spatial resolution over large area (André  
17 2016; Du et al., 2018; Haghighi et al., 2019; Miller and Shirzaei 2019; Motagh et al., 2017; Zhang et al,  
18 2019). Generally, PSI is suitable in urban areas where many man-made structures provide the vast majority  
19 of PSs. However, most of the area, running through by RLSR-HZ, is covered by farmlands, which leads to  
20 a low density of PSs. Distributed scatterers (DSs), also referred as Gaussian scatterers with random  
21 scattering mechanism (Bamler and Hart, 1998; Goodman, 1976), are widespread in natural scene and can  
22 be used in SBAS method to increase the density of measurement points (Hooper 2008; Samiei-Esfahany  
23 2017). SqueeSAR (Ferretti et al., 2011) is another advanced approach, which allows us to extract the signal  
24 from both PS and DS. SqueeSAR extracts information by exploiting all the possible interferograms rather  
25 than a set of SBAS interferograms (Ferretti et al., 2011; Samiei-Esfahany 2017; Shamshiri et al., 2018;  
26 Wang et al., 2012). This may lead to an underestimation of deformation due to large temporal baseline.

27 In this manuscript, SBAS method implemented in the Stanford method for persistent scatter (referred to  
28 as StaMPS-SB for simplicity) (Hooper 2008) is adopted and improved. StaMPS-SB has some advantages  
29 as follows. First, it has the potential for limiting the effects of topographic errors and the decorrelation by  
30 concentrating only on these interferograms with small geometric and temporal baselines (Chen et al., 2012;  
31 Goel and Adam, 2012). This contributes to the reduction of phase aliasing and thereby increasing the  
32 chances of successful phase unwrapping (Hooper 2008). Second, StaMPS-SB can operate on single look  
33 images (Hooper 2008), by which we can avoid smoothing any change in deformation and retain the  
34 deformation in the highest spatial resolution offered by the satellite. Finally, StaMPS-SB can produce the  
35 temporal evolution of deformation without any prior information about its temporal evolution (Hooper et



1 al., 2007; Hooper 2008; Sousa et al., 2011). This is very useful as there is no prior knowledge about the  
2 variations of deformation over the study region. However, standard StaMPS-SB adopts spectral filtering to  
3 discard the non-overlapping Doppler spectrum in azimuth and to reduce the geometric decorrelation in  
4 range (Hooper 2008), which leads to a coarsening of resolution and some loss of deformation information.  
5 Thus, an adaptive spatial filtering algorithm (Ferretti et al., 2011; Goel and Adam, 2011; Parizzi and Brcic,  
6 2011) is introduced to replace the spectral filtering to improve the interferometric coherence while  
7 maintaining the spatial resolution. We utilize the improved StaMPS-SB to investigate the ground  
8 deformation along RLSR-HZ using 124 C-band Sentinel-1 SAR images acquired from two tracks between  
9 July 2015 and November 2019. Having retrieved the pattern of ground deformation, the potential causes for  
10 instability along RLSR-HZ are discussed to have a better understanding of the deriving forces contributing  
11 to subsidence process. Such information is the key for the safety operation and maintenance of RLSR-HZ.

12

## 13 **2 Study area and SAR data**

### 14 2.1 Study area

15 Heze region, an important part of the North China subsidence basin, is located in the lower reaches of the  
16 Yellow River. This area has a relatively flat landform with altitude varying from 37 to 68 m and is covered  
17 by vast areas of farmland. It is characterized by semi-humid monsoon climate with a mean annual  
18 precipitation of approximately 663 mm, which is the main recharge source of groundwater. The monsoon  
19 climate makes a large seasonal variations of precipitation, i.e., most of precipitation (approximately 391  
20 mm) is concentrated in the summer (Shandong Provincial Bureau of Statistics).

21 Groundwater has been a key resource for development of agriculture and industry in Heze. More than 1  
22 billion tons of groundwater is exploited every year in the region by more than 110 deep wells in urban area  
23 and more than 137000 wells in rural area (Xu et al., 2017). Due to the abundant extraction of groundwater,  
24 the level of shallow and deep groundwater declined by more than 8 and 80 m between 1980 and 2013, with  
25 an average rate of 0.5m/yr and 5 m/yr respectively (Feng et al., 2015). Besides, Heze region is rich in coal  
26 resources with a cumulative reserve of about 10.2 billion tons spreading over an area of 2700 km<sup>2</sup>. Due to  
27 underground mining, an area more than 40 km<sup>2</sup> has suffered from serious subsidence.

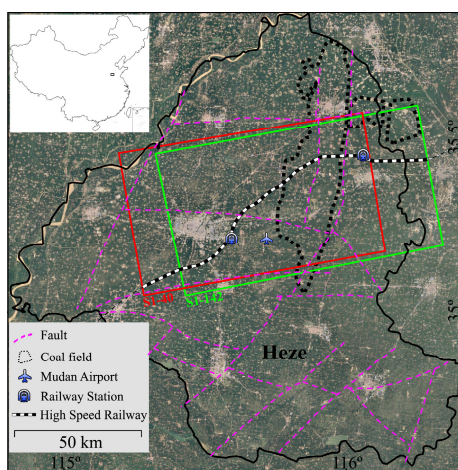
28 RLSR-HZ, with a length of about 150 km running through Heze region from southwest to northeast  
29 (shown in Fig. 1), has been under construction since December 2018 and will be operative by the end of  
30 2021. Taking advantage of ballastless track, the speed reaches up to 300 Km/h. This means that a very high  
31 stability of foundation is required for safety. It's crucial to accurately and continuously monitor the ground  
32 subsidence along RLSR-HZ to assess the risk.

### 33 2.2 SAR data

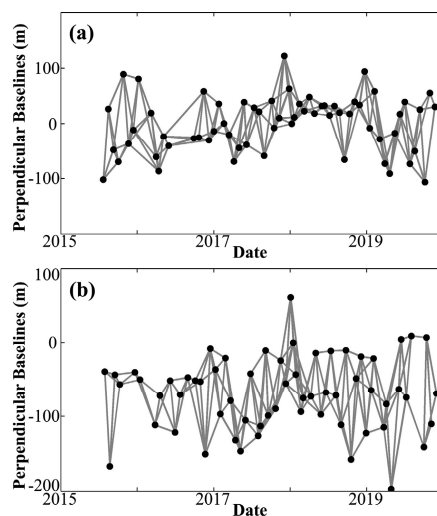
34 Our dataset includes 124 C-band Sentinel-1A SAR images in TOPS mode covering more than four years  
35 between July 2015 and November 2019. 63 of these images were collected from path 40 (referred as S1-40),



1 and 61 from path 142 (referred as S1-142). There is no descending SAR data over this region, all these  
2 images are acquired in an ascending orbit. The ground resolution of these images is approximately 20 m in  
3 azimuth and 5 m in range (Geudtner et al., 2014). Fig. 2 shows the temporal and spatial baselines of 192  
4 interferograms generated from S1-40 dataset and 171 interferograms generated from S1-142 dataset. It can  
5 be seen that the perpendicular baselines vary between -150 m and 150 m. External DEM data acquired  
6 from TanDEM-X with a pixel spacing of three arc second is used for removal of topographic phase  
7 component (Wessel et al., 2018) and for geometrical coregistration of TOPS data (Yague-Martinez et al.,  
8 2016).



9  
10 Fig. 1. Study area and outline of Sentinel-1 acquisitions superimposed on Google Earth optical image (© Google Maps).  
11 Black polygon represents the boundary of Heze region.



12  
13 Fig. 2. Connected network of interferograms for (a) S1-40 and (b) S1-142 datasets. Black dots and grey lines denote the  
14 Sentinel-1 acquisitions and interferograms, respectively.



### 1 3 Methodology

2 In this study, StaMPS-SB is improved and conducted to derive the time-series displacement from  
3 multi-temporal Sentinel-1 acquisitions. Compared with single master approach (e.g. PSI), StaMPS-SB can  
4 minimize the decorrelation effects caused by long interval of SAR acquisitions and dense farmlands over  
5 this study area (Hopper 2008).

6 First, the S1-40 dataset and S1-142 dataset are coregistered and resampled with respect to the reference  
7 images acquired on 8 January 2018 and 15 January 2018, respectively. The reference image should have the  
8 capability to maximize the quality index in coregistration strategy, which is dependent on the temporal and  
9 spatial baselines, difference of Doppler centroid and thermal noise (Hopper et al., 2007). Here, we assume  
10 the thermal noise as constant for simplicity (Hopper et al., 2007).

11 Note that, higher accuracy is required for the azimuth coregistration due to the significant Doppler  
12 frequency variation which can result in failure for traditional methods. A special strategy combining  
13 geometric coregistration and enhanced spectral diversity (ESD) (Prats-Iraola et al., 2012) technique is used  
14 in this paper. We first perform the geometric coregistration using the precise orbit with an accuracy of 5 cm  
15 and the TanDEM-X DEM with a pixel spacing of three arc second. Then, the azimuth coregistration  
16 accuracy is refined using ESD technique which exploits the differential phase in the overlap areas of  
17 consecutive bursts (Prats-Iraola et al., 2012).

18 After that, all the images (i.e., the resampled images and the reference image) are recombined with each  
19 other to generate interferograms as long as the geometric and temporal baselines are less than a predefined  
20 threshold. A small orbital separation (i.e., 150 m) is specified as the geometric baseline threshold in order to  
21 restrain the effect of spatial decorrelation noise and topographic errors. Meanwhile, a short interval (i.e., 84  
22 days) is specified as the temporal baseline threshold in order to restrain the effect of temporal decorrelation  
23 noise and accumulative deformation on wrapped phase. Then, all the interferograms are inspected to  
24 distinguish the noisy interferograms which will be excluded from the network. In addition, the temporal  
25 intervals of interferograms are not very uniform. There are some gaps being more than 84 days, which  
26 results in a disconnected network for the auto-generated interferograms. Therefore, some interferograms  
27 with high coherence are manually appended to the original stacks to form a connected network which is  
28 essential for StaMPS-SB. Finally, two connected networks containing 192 interferograms for S1-40 and  
29 171 interferograms for S1-142 are generated (shown in Fig. 2). In these networks, each image is connected  
30 to at least two other images, by which the temporal sampling rate is increased by an average factor of 2.9.  
31 Taking advantage of the adequate interferograms, the model parameters such as deformation, topographic  
32 errors and atmospheric artifacts can be estimated more accurately comparing with single master approach.

33 Generally, multilooking (Berardino et al., 2002) and spectral filtering (Hooper 2008) are the common  
34 approaches to improve the interferometric coherence and reduce the noise. Standard StaMPS-SB adopts  
35 spectral filtering to discard the non-overlapping Doppler spectrum in azimuth and to reduce the geometric



1 decorrelation in range. However, the spectral filtering operation leads to a coarsening of resolution (Hooper  
2 2008), which therefore may cause some loss of deformation information. In fact, the differences in Doppler  
3 frequency of Sentinel-1 data are only a few Hz (Yague-Martinez et al., 2016) and the common Doppler  
4 bandwidth is more than 95% in most cases. Additionally, the range bandwidth is larger than 40 MHz and  
5 almost all of the geometric baselines are shorter than 150 m. As a result no spectral filtering is applied to  
6 avoid coarsening the resolution. In contrast, an adaptive spatial filtering algorithm is introduced and  
7 implemented to improve the interferometric phase and coherence while preserving the image details  
8 (Ferretti et al., 2011; Goel and Adam, 2011; Parizzi and Brcic, 2011). We identify the statistically  
9 homogenous pixels (SHP) using the Kolmogorov-Smirnov (KS) test based on the amplitude of images. A  
10 rectangular window with a dimensions of  $19 \times 13$  (azimuth  $\times$  range) pixels is used to identify SHP, on  
11 which a spatial filtering will be implemented if the number of SHP is more than 18.

12 StaMPS-SB selects coherent targets based on the phase characteristics (Hooper 2008),

$$13 \quad \gamma_x = \frac{1}{N} \left| \sum_{i=1}^N \exp \left\{ \sqrt{-1} (\varphi_{x,i} - \tilde{\varphi}_{x,i} - \Delta\phi_{\theta,x,i}^{\mu}) \right\} \right| \quad (1)$$

14 where  $\varphi_{x,i}$  is the wrapped phase of candidate pixel  $x$  in the  $i$ th filtered interferogram.  $\tilde{\varphi}_{x,i}$  is the  
15 estimated spatially correlated terms.  $\Delta\phi_{\theta,x,i}^{\mu}$  is the spatially uncorrelated terms due to look angle error  
16 which is correlated with the perpendicular baseline.  $N$  is the number of interferograms. Candidate pixels  
17 are firstly selected using the amplitude difference dispersion specifying (a threshold of 0.6 is adopted).  
18 Then, these candidates will be filtered in small patches, such as  $50 \text{ m} \times 50 \text{ m}$ , to estimate  $\tilde{\varphi}_{x,i}$ . Finally,  
19 coherent targets will be determined though an iterative procedure estimating the noise ( $\gamma_x$ ) of each  
20 candidate by implementing the inversion of  $\Delta\phi_{\theta,x,i}^{\mu}$  as a search of parameters space. Further details on the  
21 selection method can be found in Hooper et al., (2007) and Hooper (2008).

22 Once the coherent targets have been determined, the differential interferometric phase of each coherent  
23 target is corrected using the estimated spatially uncorrelated terms (i.e.  $\Delta\phi_{\theta,x,i}^{\mu}$ ) in Eq. (1). After removal of  
24  $\Delta\phi_{\theta,x,i}^{\mu}$ , the residual phase mainly consisted of ground deformation, atmospheric artifacts and orbit error,  
25 can then be unwrapped using the three-dimensional (3-D) algorithm. Firstly, the difference phase between  
26 neighboring coherent targets is preliminarily unwrapped in time under the Nyquist assumption. A priori  
27 probability density function (PDF) can be built in each interferogram based on the unwrapped difference  
28 phase in time dimension. These PDFs are then used to search for the optimization routines of unwrapping  
29 in space to achieve the final unwrapped results (Hooper 2010). Subsequently, the time series deformation of  
30 each coherent target can be extracted by temporal and spatial filtering based on the characteristics of each



1 phase terms.

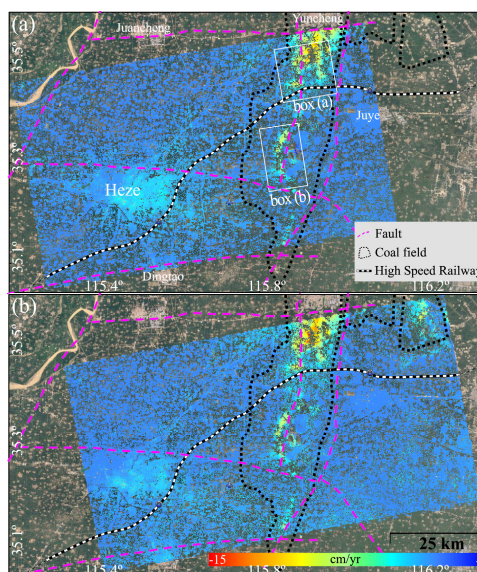
2 Note that InSAR is a relative measure to reference point. In order to derive the absolute results, the  
3 deformation of reference point should be known. However, there is no available prior information about the  
4 deformation in Heze region. In contrast to the standard procedure in StaMPS-SB which only select one  
5 reference area, we identify some possible areas not affected by deformation based on the differential phase  
6 in time series. By using multiple reference areas, we can minimize the error of the InSAR-derived  
7 deformation due to misplaced of single area (Fiaschiet al., 2017).

8

## 9 4 Results

### 10 4.1 Cross validation of the displacement

11 Fig. 3 shows the displacement rates derived from S1-40 and S1-142. The negative displacement indicates  
12 that the ground was subjected to subsidence during this period.



13

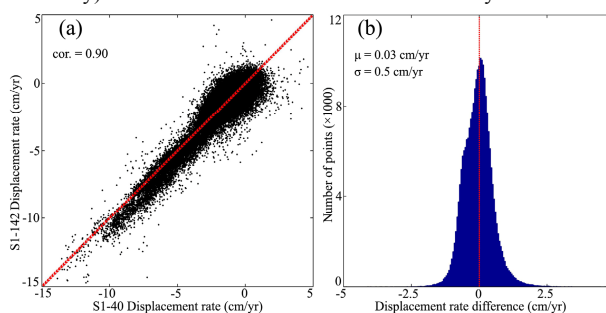
14 Fig. 3. The average rates of land displacement results from (a) S1-40 and (b) S1-142, superimposed on Google Earth optical  
15 image (© Google Maps). The two white boxes (indicated by a and b) indicate the locations of subsidence area related to  
16 underground mining shown in Fig. 9-10 and analyze in Sec. 5.2. Google Earth optical image (© Google Maps).

17 As no *in-situ* data is publicly available, we assess the consistency and precision of InSAR results by a  
18 cross comparison (shown in Fig. 4) of the displacement rates derived from the S1-40 and S1-142. Although  
19 the physical parameters of sensor is same with each other, the location of two sets of measurement points  
20 (MPs, consisting of PS and DS pixels) is slightly different due to the different geometric parameters. In  
21 order to identify the common MPs, both results from S1-40 and S1-142 are resampled to a grid with a  
22 spacing of 50 m. The displacement rates are averaged if multiple MPs are located in the same grid. Besides,  
23 the displacements are converted to vertical direction on the assumption that the horizontal displacements



1 are negligible. 232,984 common MPs are finally identified after the above procedure. Based on these  
2 common MPs, we estimate the Pearson correlation of the two measurements and get a correlation of 0.9  
3 (shown in Fig. 4a). The high correlation demonstrates the consistency of the InSAR results.

4 The variation of the difference between the two measurements illustrated in Fig. 4b provides an  
5 estimation of the precision of the InSAR results. We calculate the mean ( $\mu$ ) and standard deviation ( $\sigma$ )  
6 the difference of displacement rates. The  $\mu$  and  $\sigma$  of the difference are 0.03 cm/yr and 0.5 cm/yr,  
7 respectively. Therefore, we conclude that the two InSAR results agree well with each other and the  
8 precision (i.e., 1- $\sigma$  uncertainty) of the two measurements is about 0.5 cm/yr.



9  
10 Fig. 4. The cross-validation of InSAR results from S1-40 and S1-142. The correlation and the difference between the two  
11 measurements are shown in (a) and (b), respectively.

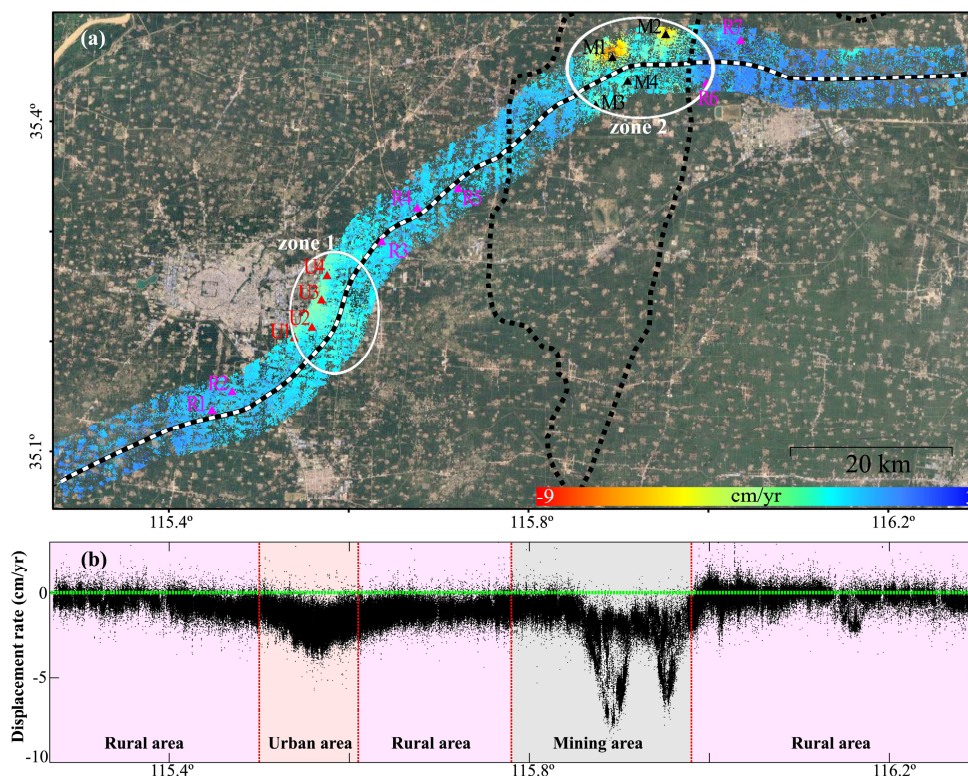
12

#### 13 4.2 Land displacement along the RLSR-HZ

14 The displacement rates within a radius of 3 km along the RLSR-HZ are illustrated in Fig. 5. The total  
15 numbers of MPs from the two sets of data are up to 312,702 and 261,397, resulting in an average density of  
16 approximately 473 and 375 MPs/km<sup>2</sup>, respectively. With the advantage of dense MPs, ground deformation  
17 along the RLSR-HZ can be represented in detail compared to conventional methods. Note that the spatial  
18 density of MPs is not homogeneous due to different ground scatterer characteristic. The MPs are evenly  
19 distributed in urban area because of dense hard objects while sparse distributed in rural area due to the  
20 vegetation cover. To increase the density of MPs, the two measurements derived from S1-40 and S1-142  
21 are both shown in Fig. 5. Thus, there are more MPs in the overlapping area.

22 Fig.5a shows the displacement rates along the designed RLSR-HZ. It can be seen that the RLSR-HZ runs  
23 through two subsidence zones (two black ellipses in Fig.5a), one of which (zone 1) is located in the east of  
24 the Heze city and another one (zone 2) in the mining area. In zone 1, the displacement rates range from -4  
25 cm/yr to -1 cm/yr. The subsidence pattern is smooth and homogeneous in space. A length of approximately  
26 20 km of RLSR-HZ will be affected by the subsidence. In contrast, the ground suffered a stronger  
27 subsidence in zone 2, and a length of approximately 15 km of RLSR-HZ will be affected. The displacement  
28 rates detected by InSAR range from -8 cm/yr to -2 cm/yr.





1  
2 Fig. 5. (a) The spatial distribution and (b) the profile of average displacement rates along RLSR-HZ. Both the results from  
3 S1-40 and S1-142 are shown, which leads to a denser MPs in the overlapping area. Two ellipses show the major subsidence  
4 area. The triangles (i.e., pink triangles named as R1-R7, red triangles named as U1-U4 and black triangle named as M1-M4)  
5 delineate the displacement features in rural area, urban area and mining area discussed in detail in Fig. 6-8, respectively. The  
6 base map in (a) is from Google Earth optical image (© Google Maps).

7 To make further investigation on the ongoing settlement, we estimate the displacement profile along the  
8 RLSR-HZ and show the results in Fig.5b. It can be seen that the deformation pattern is not homogenous  
9 along the RLSR-HZ. The ground experiences strongest subsidence in the underground mining area,  
10 followed by the urban area. We also observe slightly deformation in rural area, where the displacement  
11 rates primarily are in the range of -2 cm/yr to 1 cm/yr. However, another subsidence areas with the  
12 maximum rates up to -3 cm/yr appear near the 116.16°. This area is offset from the coalfield by 3.5 km, so  
13 the subsidence phenomenon there might be related to the underground mining.

14

#### 15 4.3 Heze Mudan Airport

16 Another remarkable subsidence feature is a localized area around the Heze Mudan Airport (HMA)  
17 (shown in Fig. 3). HMA has been under construction since 2017 and will open and serve Shandong with  
18 domestic flights in 2020 according to the schedule. InSAR deformation maps (Fig. 3) show a subsidence  
19 feature near the airport with a maximal displacement rate of approximately -3 cm/yr. The ancillary facilities



1 of the airport, such as the runway and terminal buildings, are also affected by nonuniform subsidence range  
2 from -3 cm/yr to -0.5 cm/yr.

3

#### 4 **5 Discussion**

5 Several possible causes, including natural factors and anthropogenic activities, could be related to this  
6 deformation observed in Heze. Tectonic movement and underground caves can cause ground deformation.  
7 However, the high displacement rates, which exceed 5 cm/yr at many locations, are not in agreement with  
8 the tectonic movement rates which are estimated to be less than 0.5 cm/yr (Guo et al., 2019). In addition,  
9 there are no known underground caves associated with sinkholes or karst landforms in this region. In  
10 contrast, close inspections of the location of subsidence area and considering the underground mining  
11 coupled with the decreasing hydraulic heads in this region, we infer that this deformation is mainly caused  
12 by extensive extraction of groundwater and coal mine. This will be elaborated more in the following.

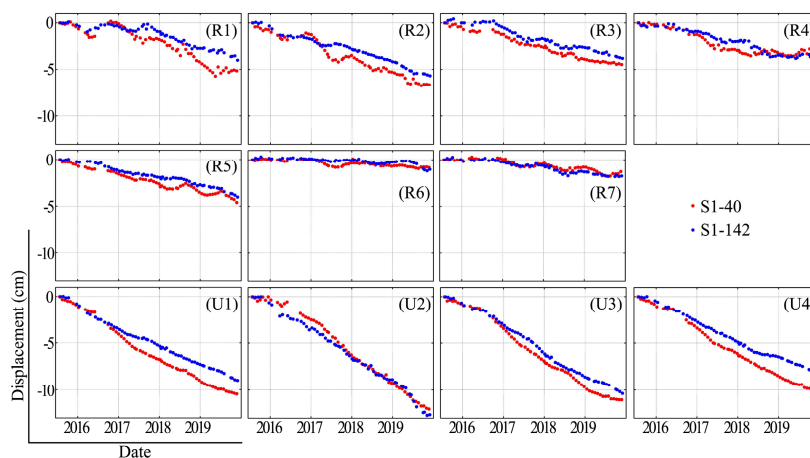
13

#### 14 5.1 Correlation between ground deformation and groundwater withdraw

15 Groundwater has been exploited for agricultural irrigation, industrial and residential use in Heze region  
16 since the early 1970s. Long-term exploitation of groundwater, will brings about a compaction of the fine  
17 clay layer, and finally results in the ground subsidence. Previous researches indicate that the excessive  
18 groundwater withdrawal is one of the main reasons of ground deformation in this area (Hu et al., 2004; Guo  
19 et al., 2019; Xue et al., 2005).

20 To better understand the ground motion, the time series displacements of MPs located within a 50 m  
21 radius around 11 points (marked by red and pink triangles in Fig .5) are shown in Fig .6. It can be seen that  
22 most of these locations suffer from ground subsidence during the period from July 2015 to November 2019.  
23 It suggests that the groundwater is still excessively exploited and the groundwater recharge is insufficient to  
24 supply the exploitation. Xu et al., (2017) pointed out that more than 1 billion tons of groundwater is over  
25 extracted annually by more than 137000 wells in Heze region.

26 Besides, Fig .6 shows that the behavior of the time series displacement significantly differs at rural area  
27 and urban area. Comparing with rural area, the ground experiences more serious subsidence in urban area.  
28 One reason for the large settlement in urban area is that the deep groundwater (over 200 m depth) is  
29 massively extracted to meet the industrial, except for shallow groundwater to domestic use. Approximately  
30 0.16 billion tons of groundwater is over extracted annually by more than 110 deep wells in urban area of  
31 Heze (Xu et al., 2017; Shandong Provincial Bureau of Statistics). The level of deep groundwater declined  
32 by more than 100 m between 1980 and 2018 (Feng et al, 2015; Yue 2020). However, many thick clay  
33 layers over the confined aquifer restrict the flow for aquifer recharging from precipitation in vertical  
34 direction. Meanwhile, the recharge rates of deep groundwater in the horizontal direction, i.e., running off  
35 along the topography from west to east, is very slow (Qiao and Lin 2006; Zhang 2013).



1

2 Fig. 6. Time series displacement of MPs located in rural area (R1-R7) and urban area (U1-U4) shown in Fig. 5.

2

3 As the detailed information of aquifer are not public, we cannot investigate the detailed relationship  
4 between the subsidence and the groundwater level. However, the precipitation is the mainly recharge  
5 source of shallow groundwater (accounting for 85% of the total supply) in this region and directly  
6 determine the level of shallow groundwater (Jia 2015; Ma and Feng, 2014; Yu et al 2001). Therefore, we  
7 switch to investigate the relationship between the subsidence and the precipitation.

8 The precipitation from July 2015 to December 2019 is presented in Fig. 7a. We can infer the variation of  
9 shallow groundwater according to the precipitation. Generally, the precipitation, exploitation and  
10 evaporation of groundwater are little from January to February in Heze region. During this period, the  
11 groundwater level is a relatively stable and rises slowly until the beginning of March. In addition, the freeze  
12 of water contained in the soil due to the low temperature, can also increase the volume and result in an  
13 inflation. From March to June, the little precipitation and massive extraction of groundwater to irrigate  
14 crops result in a continuous declining of groundwater level until the beginning of the rainy season. The  
15 water level rebounds from July to September due to lots of precipitation, and maintains a relatively stable  
16 due to the decreasing of extraction during October to December (Jia 2015).

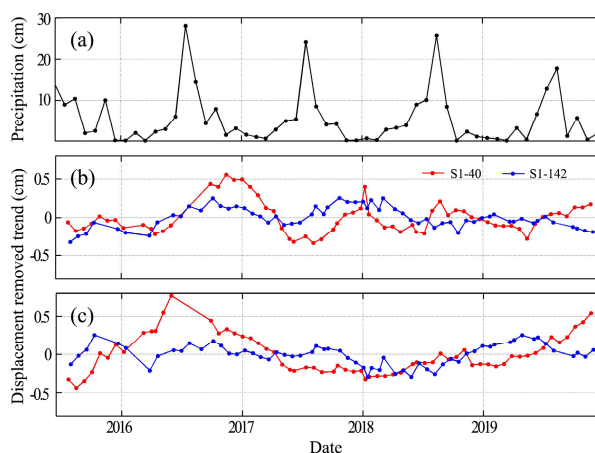
17 The average time series displacement, after removing its trend, of all points located in rural area is used  
18 as an average representation of the variations of rural area and shown in Fig. 7b, whilst the average  
19 variations of urban area shown in Fig. 7c.

20 The deviation in rural area (Fig. 7b) indicates that the ground fluctuates by approximately  $\pm 0.5$  cm with a  
21 significantly seasonal variation. The seasonal variation may be related to the seasonal variation of aquifer  
22 water level which is determined by the seasonal precipitation. In addition, as shown in Fig. 7b, the  
23 variations of displacement in rural areas have a significant correlation with precipitation with a time lag of  
24 approximately two months. We hypothesize that the ground subsidence is caused by both the hydraulic  
25 head change and the seasonal groundwater variations. And the time lag is induced by the groundwater level



1 increases arising from the seasonal precipitation.

2 In contrast, Fig. 7c shows that there is no straightforward relationship between the precipitation and the  
3 variations of displacement in urban area. It may due to the extraction of deep rather than shallow  
4 groundwater as the deep groundwater is difficult to recharge owing to the complicated geological  
5 conditions in this region (Qiao and Lin 2006; Zhang 2013). Zhang et al., (2018) found that the subsidence  
6 has a significant correlation (up to 0.96) with the declining of deep groundwater level in another city near  
7 Heze.



8

9 Fig. 7.(a) Monthly precipitation for the Heze region during July 2015 and December 2019. After removing the linear trend,  
10 the average of residual time series displacement of (b) R1-R7 in rural area and (b) U1-U4 in urban area.

11

## 12 5.2 Correlation between ground deformation and underground mining

13 In Fig. 8, the time series displacements at four locations (M1~M4 in Fig. 5) above coal field are shown.  
14 Fig. 5 and Fig. 8 show that the accumulative subsidence above coal does not exceed 50 cm during more  
15 than four years. In addition, Fig. 8 reveals a significant linear displacement trend. In fact, the  
16 mining-induced subsidence is generally nonlinear with high rates, which can reach up to several meters in a  
17 short time (e.g, several months). These characteristics indicate that the subsidence near M1~M4 may not be  
18 directly induced by underground mining.

19 Note that the underground mining inevitably produces many fracture fields which may be interconnected  
20 with the faults, forming a large interconnected network. The groundwater will flow into the working planes  
21 through fractures and be drained out (Rapantova et al., 2007; Xu et al., 2018), which finally results in the  
22 ground subsidence. In addition, underground mining may destroy the stability of faults and induce the  
23 faults slipping (Islam and Shinjo, 2009; Wang et al., 2016; Zhang et al., 2018), which can also lead to  
24 ground subsidence.

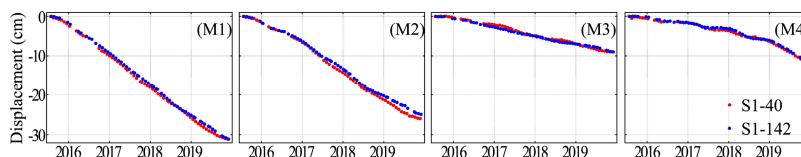
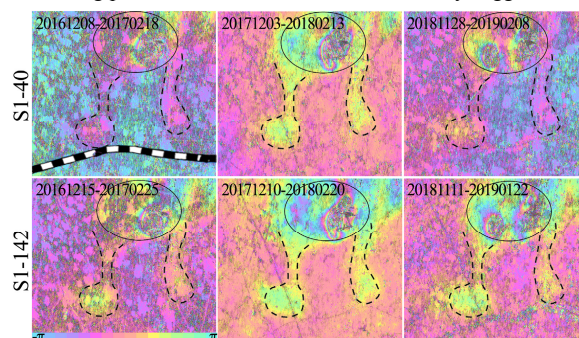


Fig. 8. Time series displacement of MPs located in mining area (M1-M4) shown in Fig. 5.

1  
 2  
 3 In Fig. 9, six interferograms of box (a) in Fig. 3a are shown. It is observed that there are several active  
 4 subsidence areas, represented by dense fringes (ellipses in Fig. 9), locate in 5~8 km north of M1 and M2.  
 5 The loss of signal in the central of these subsidence areas is probably due to the displacement being too  
 6 large to be detected by MT-InSAR with the C-band Sentinel-1 data. This conforms to the mining-induced  
 7 displacement field which presents a bowl-shaped subsidence pattern, as observed in other studies (He et al.,  
 8 1994; Litwiniszyn 1956; Zhu et al., 2020). The dense fringes, i.e., strong deformation, suggests there is  
 9 active underground mining just below this subsidence basin (referred as primary subsidence basin and  
 10 denoted by ellipses in Fig. 9). In contrast, all the six interferograms and the corresponding displacement  
 11 rates shown in Fig. 3 reveal a relatively slight subsidence near M1 and M2 (referred as secondary  
 12 subsidence basin) in comparison to the primary subsidence basin. Close inspections of the distribution of  
 13 fringes in Fig. 9, the ground deformation seems to progress to M1 and M2 area along two ‘galleries’  
 14 (dashed line in Fig. 9). A plausible explanation of this deformation near M1 and M2 could be the  
 15 groundwater outflow to working panels and is drained out, which finally triggers the ground subsidence.

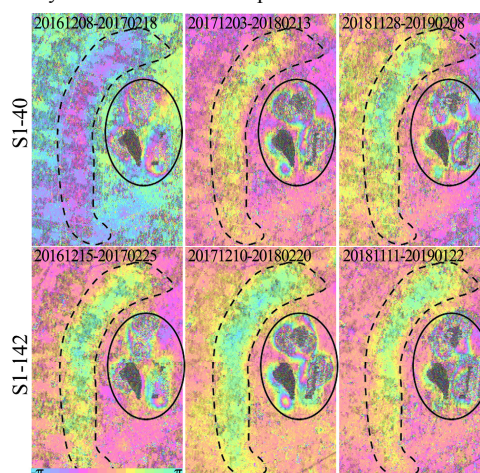


16  
 17 Fig. 9 .Example of interferograms produced from S1-40 and S1-142 of box (a) in Fig. 3. The ellipses show the primary  
 18 subsidence area induced by underground mining. One color fringe stands for approximately 2.8 cm displacement in the LOS.  
 19 The dashed lines show the secondary subsidence area caused by complicated factors, e.g, groundwater drain out and/or fault  
 20 activation due to underground mining.

21 In addition, a similar phenomenon is observed in an area (box (b) in Fig.3a) 5-11 km south of RLSR-HZ.  
 22 Fig. 10 shows six interferograms of this area. In the right (ellipses in Fig. 10), the dense fringes in this  
 23 primary subsidence area imply active underground mining. However, an arc-shape secondary subsidence  
 24 area (dashed line in Fig. 11) with a length of about 14 km presents in 3 km to the left of the primary  
 25 subsidence area. The arc-shape subsidence does not agree with the law of the ground movement induced by  
 26 underground mining. Fig.3 shows the arc-shape subsidence is consistent with the fault, which implies that



1 the underground mining causes the fault activation and results in ground deformation. Unfortunately, it  
2 difficult to investigate the interactions between the underground mining, fault activation and ground  
3 deformation, as we do not have detailed information, such as the distribution of unknown faults and  
4 abandoned mines, the relative position of the faults and mining sites. Nevertheless, the concomitant ground  
5 deformation (i.e., secondary subsidence basin) induced by underground mining reminds us that it must very  
6 careful to extract coal, especially when there are widespread faults.



7  
8 Fig. 10 . Example of interferograms produced from S1-40 and S1-142 of box (b) in Fig. 3. The ellipses show the primary  
9 subsidence area induced by underground mining. One color fringe stands for approximately 2.8 cm displacement in the LOS.  
10 The dashed lines show the secondary subsidence area caused by complicated factors, e.g, groundwater drain out and/or fault  
11 activation due to underground mining.

12

## 13 6 Conclusion

14 This study investigates the time series displacement for the period of 2015-2019 using MT-InSAR based  
15 on two sets of Sentinel-1A dataset over Heze region. The two independent MT-InSAR results are agree well  
16 with each other with 1- $\sigma$  uncertainty of approximately  $\pm 0.5$  cm/yr. Focus on the ground displacement along  
17 RLSR-HZ, we find that there are two main ground subsidence zones:

- 18 - One subsidence zone is located in the east of Heze city ( $115.5^{\circ}\text{E} \sim 115.6^{\circ}\text{E}$ ) with a displacement  
19 rates ranging from  $-4$  cm/yr to  $-1$  cm/yr. A length of approximately 20 km of RLSR-HZ will be  
20 affected by this subsidence.
- 21 - One subsidence zone is located in the coal field ( $115.8^{\circ}\text{E} \sim 116.0^{\circ}\text{E}$ ) with a displacement rates  
22 ranging from  $-8$  cm/yr to  $-2$  cm/yr. A length of approximately 15 km of RLSR-HZ will be affected  
23 by this subsidence.

24 Considering the previous investigation coupled with information of human activities, we conclude that  
25 the subsidence is mainly caused by extraction of groundwater and underground mining:

- 26 - Combining the known previous investigations and the monthly precipitation, we find two patterns of



1 subsidence: a long-term subsidence due to the extraction of deep groundwater mainly in the urban  
2 area, and a short-term variations related to the seasonal precipitation mainly in the rural area.

3 - Underground mining is another cause of ground subsidence, which can reach up to several meters.  
4 However, we found an interesting phenomenon that a secondary subsidence basin presents farther  
5 away (about 3-7 km) from the primary subsidence basin (Fig. 9 and 10). Considering the known  
6 faults and the unknown mining-induced fracture fields, we infer that the secondary subsidence is  
7 very probably caused by the groundwater outflow and fault instability due to mining, rather than  
8 being directly caused by mining. It will be interesting to further investigate the cause of secondary  
9 subsidence when more data become available.

10 It is very difficult to restore the surface elevation and the foundation stability after extracting deep  
11 groundwater and coal mine. The ongoing subsidence will seriously damage the infrastructures of RLSR-HZ,  
12 particularly when the RLSR-HZ will be operational by the end of 2021. Effective management in  
13 groundwater and coal mine is in urgent need to implement. In addition, it is very meaningful to continue  
14 the monitoring of ground deformation along RLSR-HZ using multiple SAR data.

15

16 **Data availability.** Sentinel-1A/B data are available at <https://scihub.copernicus.eu/>. TanDEM-X are freely downloaded from  
17 <https://sso.eoc.dlr.de/eoc/auth/login?service=https://download.geoservice.dlr.de/TDM90/files/>. The monthly precipitation are  
18 available at <http://data.cma.cn/>. The information about the annual exploitation of groundwater is provided by Shandong  
19 Provincial Bureau of Statistics from <http://www.stats-sd.gov.cn/col/col6279/index.html?uid=29225&pageNum=1>.

20

21 **Author contributions.** CZ initiated the study and wrote the manuscript. WW provided python scripts for analysis. CZ and  
22 MM analyzed the data. MM, LZ, ZJ and SL provided advice and reviewed the manuscript.

23

24 **Competing interests.** The authors declare that they have no conflict of interest.

25

26 **Acknowledgements.** Thanks go to the StaMPS software that can be downloaded from  
27 <http://homepages.see.leeds.ac.uk/~earahoo/stamps/index.html>. The authors would also like to thank the reviewers for their  
28 careful work.

29

30 **Financial support.** This research was supported by the National Natural Science Foundation of China (41901373 and  
31 41877283), the Natural Science Foundation of Hunan Province (2019JJ50190). The authors would also like to thank the  
32 reviewers for their careful work. Thanks go to the StaMPS software that can be downloaded from  
33 <http://homepages.see.leeds.ac.uk/~earahoo/stamps/index.html>.

34

## 35 References

36 André Vervoort.: Surface movement above an underground coal longwall mine after closure. *Natural Hazards and Earth*



- 1     *System Sciences*,16(9): 2107-2121, 2016.
- 2     Berardino, P., Fornaro, G., Lanari, R., and Sansosti, E.: A New Algorithm for Surface Deformation Monitoring Based on
- 3         Small Baseline Differential SAR Interferograms, *IEEE Transactions on Geoscience and Remote Sensing*, 40: 2375-2383,
- 4         2002. doi:10.1109/TGRS.2002.803792.
- 5     Bamler, R., and Hartl, P.: Synthetic aperture radar interferometry. *Inverse Problems*, 14, R1-R54, 1998.
- 6     Chen, F. L., Lin, H., Li, Z., Chen, Q., and Zhou, J.M., Interaction between permafrost and infrastructure along the
- 7         Qinghai-Tibet Railway detected via jointly analysis of C- and L-band small baseline SAR interferometry, *Remote Sensing*
- 8         of Environment, 123: 532-540, 2012. doi:10.1016/j.rse.2012.04.020
- 9     Cui, Z. D.: *Land Subsidence Induced by the Engineering-Environmental Effect*. Springer, 2018.
- 10    Du, Z. Y., Ge, L. L., Ng, H. M. , and Li, X. J.: Investigation on mining subsidence over Appin-West Cliff colliery using
- 11         time-series SAR interferometry. *International Journal of Remote Sensing*,39(5): 1528-1547, 2018.
- 12    Feng, C. C., Ma, X. F., and Huang, W. F.: Analysis on land subsidence survey and trend in Heze city[C], 13<sup>th</sup> Geoscience and
- 13         Technology Forum of East China, Nanchang, Jiangxi, 1 November 2015, 383-387, 2015.
- 14    Ferretti, A., Fumagalli, A., Novali, F., Prati, C., Rucci, A., and Rucci, A.: A new algorithm for processing interferometric
- 15         data-stacks: squeeSAR. *IEEE Transactions on Geoscience and Remote Sensing*, 49(9), 3460-3470, 2011.
- 16    Ferretti, A., Prati, C., and Rocca, F.: Non-linear Subsidence Rate Estimation Using Permanent Scatterers in Differential SAR
- 17         Interferometry, *IEEE Transactions on Geoscience and Remote Sensing*, 38: 2202-2212, 2000. doi:10.1109/36.868878.
- 18    Ferretti, A., Prati, C., and Rocca, F.: Permanent Scatterers in SAR Interferometry, *IEEE Transactions on Geoscience and*
- 19         *Remote Sensing*, 39: 8-20, 2001. doi:10.1109/36.898661.
- 20    Fiaschi, S., Closson, D., Karaki, N. A., Pasquali, P., Riccardi, P., and Floris, M.: The complex karst dynamics of the Lisan
- 21         Peninsula revealed by 25 years of DInSAR observations. *Dead Sea, Jordan. ISPRS Journal of Photogrammetry and*
- 22         *Remote Sensing*, 130, 358-369, 2017. doi.org/10.1016/j.isprsjprs.2017.06.008
- 23    Geudtner, D., Torres, R., Snoeij, P., Davidson, M., and Rommen, B.: Sentinel-1 System capabilities and applications. In:
- 24         Proceedings of IEEE International Conference on Geoscience and Remote Sensing Symposium, IGARSS 2014, Quebec,
- 25         Canada, 13-18 July, pp. 1457-1460, 2014.
- 26    Goel, K., and Adam, N.: High resolution differential interferometric stacking via adaptive spatial phase filtering. In:
- 27         Proceedings of IEEE International Conference on Geoscience and Remote Sensing Symposium, IGARSS 2011, Vancouver,
- 28         Canada, 24-29 July, pp. 1341-1344, 2011.
- 29    Goel, K., and Adam, N.: An advanced algorithm for deformation estimation in non-urban areas. *ISPRS Journal of*
- 30         *Photogrammetry and Remote Sensing*, 73, 100-110, 2012. doi.org/10.1016/j.isprsjprs.2012.06.001
- 31    Goodman, J. W.: Some fundamental properties of speckle, *Journal of the Optical Society of America*, 66, 1145-1150, 1976.
- 32    Guo, C. X., Nie, J. L., Tian, J., Wang, W. L., Cheng, C. L., Wang, B., Yin, H. F., and Zhang, H. P.: Vertical ground
- 33         displacements in the Shandong Province derived from long-term GNSS and leveling surveying, *Advances in Space*
- 34         *Research*, 64, 1388-1397, 2019.
- 35    Haghighi, M.H., and Motagh, M.: Ground surface response to continuous compaction of aquifer system in Tehran, Iran:
- 36         Results from a long-term multi-sensor InSAR analysis. *Remote Sensing of Environment*,221: 534-550, 2019.
- 37    He, G. Q., Yang, L., Lin, G. D., Jia, F. C., and Hong, D.: *Mining Subsidence Engineering*, Xuzhou, China: Press China Univ.
- 38         *Mining Technol.*, 1994.
- 39    Hooper, A.: A Multi-Temporal InSAR Method Incorporating Both Persistent Scatterer and Small Baseline Approaches,
- 40         *Geophysical Research Letters*, 35: L16302, 2008. doi:10.1029/2008GL034654.
- 41    Hooper, A.: A statistical-cost approach to unwrapping the phase of InSAR time series. *Proc. Fringe 2009 Workshop*, Frascati,
- 42         Italy, 30 November–4 December. 5 p, 2010.
- 43    Hooper, A., Segall, P., and Zebker, H.: Persistent Scatterer Interferometric Synthetic Aperture Radar for Crustal Deformation
- 44         Analysis, with Application to Volcán Alcedo, Galápagos, *Journal of Geophysical Research*, 112: B07407, 2007.





- 1 doi:10.1029/2006JB004763.
- 2 Hu, R. L., Yue, Z. Q., Wang, L. C., and Wang, S. J.: Review on current status and challenging issues of land subsidence in  
3 China. *Engineering Geology*, 76, 65-77, 2004.
- 4 Hung, W. C., Hwang, C., Chen, Y. A., Chang, C. P., Yen, J. Y., Hooper, A., and Yang, C. Y.: Surface deformation from  
5 persistent scatterers interferometry and fusion with leveling data: a case study over the choushui river alluvial fan,  
6 taiwan. *Remote Sensing of Environment*, 115(4): 957-967, 2011.
- 7 Islam, M. R., and Shinjo, R.: Mining-induced fault reactivation associated with the main conveyor belt roadway and safety of  
8 the Barapukuria Coal Mine in Bangladesh: Constraints from BEM simulations, *International Journal of Coal Geology*,  
9 79(4): 115-130, 2009. doi.org/10.1016/j.coal.2009.06.007
- 10 Jia, P. Y.: Investigation and evaluation of groundwater environment in Heze City, Zhihuai, (1): 83-84, 2015.
- 11 Kampes, B.: *Radar Interferometry: Persistent Scatterer Technique*, Springer, 2006.
- 12 Litwiniszyn, J.: Application of the equation of stochastic processes to mechanics of loose bodies, *Archives Mechanics*, 8(4):  
13 393-411, 1956.
- 14 Ma, L., and Feng, C. C.: Analysis on sustainable utilization and exploitation potentiality of shallow groundwater resources in  
15 Heze Yellow River flood plain areas, *Shandong Land and Resources*, 30(2): 43-45, 2014.
- 16 Miller, M. M., and Shirzaei, M.: Land subsidence in Houston correlated with flooding from Hurricane Harvey. *Remote  
17 Sensing of Environment*, 225, 368-378, 2019.
- 18 Mora, O., Mallorqui, J.J., and Broquetas, A.: Linear and nonlinear terrain deformation maps from a reduced set of  
19 interferometric SAR images, *IEEE Transactions on Geoscience and Remote Sensing*, 41(10): 2243-2253, 2003.
- 20 Motagh, M., Shamshiri, R., Haghighi, M. H., Wetzel, H. U., Akbari, B., Nahavandchi, H., Roessner, S. and Arabi, S.:  
21 Quantifying groundwater exploitation induced subsidence in the Rafsanjan plain, southeastern Iran, using InSAR  
22 time-series and in situ measurements. *Engineering geology*, 218, 134-151, 2017.
- 23 Parizzi, A., and Brcic, R. . (2011). Adaptive InSAR Stack Multilooking Exploiting Amplitude Statistics: A Comparison  
24 Between Different Techniques and Practical Results. *IEEE Geoscience and Remote Sensing Letters*, 8(3): 441-445, 2011.
- 25 Prats-Iraola, P., Scheiber, R., Marotti, L., Wollstadt, S., and Reigber, A.: TOPS Interferometry With TerraSAR-X, *IEEE  
26 Transactions on Geoscience and Remote Sensing*, 50(8), 3179-3188, 2012.
- 27 Qiao, G., and Lin, H. J.: Evaluation and analysis of deep groundwater in Heze City, *Shandong Water Resources*, (8): 99-100,  
28 2006.
- 29 Rapantova, N., Grmela, A., Vojtek, D., Halir, J., and Michalek, B.: GROUNDWATER FLOW MODELLING  
30 APPLICATIONS IN MINING HYDROGEOLOGY, IMWA Symposium 2007: Water in Mining Environments, 27-31 May  
31 2007, Cagilari, Italy, 2007.
- 32 Samiei-Esfahany, S.: Exploitation of distributed scatterers in synthetic aperture radar interferometry. PhD thesis, Delft  
33 University of Technology, 2017.
- 34 Shamshiri, R., Nahavandchi, H., Motagh, M., and Hooper, A.: Efficient ground surface displacement monitoring using  
35 sentinel-1 data: integrating distributed scatterers (DS) identified using two-sample t-test with persistent scatterers (PS).  
36 *Remote Sensing*, 10(5), p.794, 2018. doi.org/10.3390/rs10050794
- 37 Shandong Provincial Bureau of Statistics.: *Shandong Statistical Yearbook*, Beijing, China Statistics Press, 2010-2019.
- 38 Sousa, J. J., Hooper, A. J., Hanssen, R. F., Bastos, L. C., and Ruiz, A. M.: Persistent Scatterer InSAR: A comparison of  
39 methodologies based on a model of temporal deformation vs. spatial correlation selection criteria. *Remote Sensing of  
40 Environment*, 115, 2652-2663, 2011. doi:10.1016/j.rse.2011.05.021
- 41 Wang, H. Q.: Mining subsidence monitoring around Longgu coal mine based on remote sensing, *Advanced Materials  
42 Research*, 1010-1012: 489-495, 2014.
- 43 Wang, H. W., Jiang, Y. D., Xue, S., Mao, L. T., Lin, Z. N., Deng, D. X., and Zhang, D. Q.: Influence of fault slip on  
44 mining-induced pressure and optimization of roadway support design in fault-influenced zone, *Journal of Rock mechanics*



- 1 and Geotechnical Engineering, 8(5): 660-671, 2016. doi.org/10.1016/j.jrmge.2016.03.005
- 2 Wang, Y., Zhu, X.X., and Bamler, R.: Retrieval of phase history parameters from distributed scatterers in urban areas using  
3 very high resolution SAR data. *ISPRS J. Photogramm. Remote Sensing*, 73, 89–99, 2012.
- 4 Wessel, B., Huber, M., Wohlfart, C., Marschall, U., Kosmann, D., and Roth, A.: Accuracy assessment of the global  
5 TanDEM-X Digital Elevation Model with GPS data. *ISPRS Journal of Photogrammetry and Remote Sensing*, 139,  
6 171-182, 2018. doi.org/10.1016/j.isprsjprs.2018.02.017
- 7 Xu, J. Y., Mao, L., Zhang, T., and Wang, Z. S.: The development and utilization of water resources and security assurance  
8 planning study in Heze City, China *Population, Resources and Environment*, 27(11): 200-203, 2017.
- 9 Xu, S. Y., Zhang, Y. B., Shi, H., Wang, K., Geng, Y. P., and Chen, J. F.: Physical Simulation of Strata Failure and Its Impact on  
10 Overlying Unconsolidated Aquifer at Various Mining Depths, *Water*, 10(5): 650-667, 2018. doi:10.3390/w10050650
- 11 Xue, Y. Q., Zhang, Y., Ye, S. J., Wu, J. C., and Li, Q. F.: Land subsidence in china. *Environmental Geology*, 48(6), 713-720,  
12 2005.
- 13 Yague-Martinez, N., Prats-Iraola, P., Rodriguez, G. F., Brcic, R., Shau, R., Geudtner, D., Eineder, M., and Bamler, R.:  
14 Interferometric Processing of Sentinel-1 TOPS Data. *IEEE Transactions on Geoscience and Remote Sensing*, 54(4),  
15 2220-2234, 2016.
- 16 Yang, S. Y., Yang, H. C., Jing, C. Q., Yue, X. L., and Jie, J.: Comprehensive Control of the Coal Mine Subsidence Area: A  
17 Case of the Subsidence Area of Chenman Village in Heze of Shandong Province, China *Population, Resources and  
18 Environment*, 20(5): 194-196, 2010.
- 19 Yu, C. J., Jia, P. Y., Lv, S. G., Yuan, X. A., and Zang, X. L.: Analysis of shallow groundwater in Heze city, Shandong *Water  
20 Resources*, (4): 14-15, 2001.
- 21 Yue, J. G.: Analysis on the current situation and causes of land subsidence along the Lunan high speed railway, *Railway  
22 Investigation and Surveying*, (2): 60-65, 2020.
- 23 Zhang, H., Dong, M., Ma, J., Liu, Y. H., and Liu, K.: Relationship between the deep groundwater exploitation and land  
24 subsidence in Changyi district of Shandong province, China *Earthquake Engineering Journal*, 40, 214-218, 2018.  
25 doi:10.3969/j.issn1000-0844.2018.Supp.214
- 26 Zhang, L. L.: Study on land subsidence prevention and control along the Jingjiu Railway (Shandong Section) [D], Beijing,  
27 China University of Geosciences (Beijing), 2013.
- 28 Zhang, Q. Y., Li, Y. S., Zhang, J. F., and Luo, Y.: InSAR Technique Applied to the Monitoring of the Qinghai-Tibet Railway,  
29 *Natural Hazards and Earth System Sciences*, 19, 2229–2240, 2019. doi.org/10.5194/nhess-19-2229-2019.
- 30 Zhang, Y. H., Underschultz, J., Langhi, L., Mallants, D., and Strand, J.: Numerical modelling of coal seam depressurization  
31 during coal seam gas production and its effect on the geomechanical stability of faults and coal beds, *International Journal  
32 of Coal Geology*, 195, 1-13, 2018. doi.org/10.1016/j.coal.2018.05.008
- 33 Zhu, C. G., Wang, Z. S., Li, P. X., Motagh, M., Zhang, L. Y., Jiang, Z. L., and Long, S. C.: Retrieval and Prediction of  
34 Three-Dimensional Displacements by Combining the DInSAR and Probability Integral Method in a Mining Area, *IEEE  
35 Journal Of Selected Topics In Applied Earth Observations And Remote Sensing*, 2020.  
36 doi.org/10.1109/JSTARS.2020.2978288
- 37